

## Full length article

## Synthesis and stabilization of a new phase regime in a Mo-Si-B based alloy by laser-based additive manufacturing

S.K. Makineni<sup>\*</sup>, A.R. Kini, E.A. Jägle, H. Springer, D. Raabe, B. Gault<sup>\*\*</sup>

Department of Microstructure Physics and Alloy Design, Max-Planck-Institut für Eisenforschung GmbH, 40237, Düsseldorf, Germany

## ARTICLE INFO

## Article history:

Received 19 November 2017

Received in revised form

20 March 2018

Accepted 20 March 2018

Available online 27 March 2018

## Keywords:

Laser additive manufacturing (LAM)

Mo-Si-B based alloy

Oxide dispersion

Transmission electron microscopy (TEM)

Atom probe tomography (APT)

## ABSTRACT

Mo-Si-B alloys are potential creep resistant materials for accessing harsh loading scenarios beyond Ni-based superalloys due to their excellent mechanical performance at ultra-high temperatures (> 1200 °C). Here, we report on the fabrication through laser additive manufacturing of a Mo rich Mo-Si-B alloy with and without dispersion of oxide ( $\text{La}_2\text{O}_3$ ) particles. The major phase in the solidified material is dendritic  $\alpha$ -Mo. The inter-dendritic regions contain a mixture of the  $\text{Mo}_5\text{Si}_3$  (T1) +  $\text{Mo}_5\text{SiB}_2$  (T2) phases, and not the expected equilibrium  $\text{Mo}_3\text{Si}$  +  $\text{Mo}_5\text{SiB}_2$  (T2) phases. This combination of phases is shown to yield improved high temperature creep resistance but was only accessible through by addition of Nb, W or Ti that substitute Mo in the intermetallic phases. Whereas here it is attributed to the large under-cooling in the small melt pool produced during laser processing. We show that this phase mixture, upon annealing, is stable at 1200 °C for 200 h. We also demonstrate successful dispersion of oxide particles mainly in the inter-dendritic regions leading to a high indentation fracture toughness of  $\sim 18 \text{ MPa}\sqrt{\text{m}}$  at room temperature. Toughening originates from crack trapping in the ductile  $\alpha$ -Mo and the formation of micro-cracks and crack deflection in the vicinity of oxide particles.

© 2018 Acta Materialia Inc. Published by Elsevier Ltd. All rights reserved.

## 1. Introduction

Refractory based Mo-Si-B alloys are promising high temperature structural alloys, especially for components in gas-turbine engines. They are able to withstand higher temperatures compared to existing single crystal Ni-based superalloys that are limited to regimes up to  $\sim 1200$  °C, i.e. above 90% of their respective melting points [1–4]. The prime motivation to design Mo-Si-B based alloys is to increase the turbine's operating temperature, thereby improving fuel efficiency. The tolerance of these alloys against strong oxidation at temperatures above 1300 °C is due to the formation of a boron-rich borosilicate layer on the surface [5–7].

In this Mo-Si-B system, two main polyphase regimes have been explored as shown in Fig. 1: (1)  $\alpha$ -Mo +  $\text{Mo}_3\text{Si}$  +  $\text{Mo}_5\text{SiB}_2$  (T2 phase), also known as “Berczik's triangle” [5,6] and (2)  $\text{Mo}_3\text{Si}$  +  $\text{Mo}_5\text{Si}_3$  (T1 phase) +  $\text{Mo}_5\text{SiB}_2$  (T2 phase). Materials in both phase regimes show rather brittle fracture behavior at room temperature. However, alloys from regime (1) show slightly better

mechanical response [4,8–10], as the presence of a ductile  $\alpha$ -Mo solid solution phase renders the alloy more damage tolerant compared to alloys in regime (2) containing only intermetallic phases [11–13]. For alloys based on regime (1), the  $\alpha$ -Mo solid solution matrix provides intrinsic toughening at room temperature by crack blunting and trapping mechanisms. Thus, the fracture toughness can be tuned from  $\sim 5 \text{ MPa}\sqrt{\text{m}}$  to  $\sim 20 \text{ MPa}\sqrt{\text{m}}$  depending on the  $\alpha$ -Mo volume fraction [14,15]. In molybdenum alloys, it was shown that rare earth oxide dispersion leads to an increase in the fracture toughness by as much as 400% depending upon the distribution of oxide particles [16]. This distribution can be tuned by adopting specific processing routes such as conventional sintering of solid Mo based powders with solid oxide particles (S-S doping) or with rare earth liquid solution (S-L doping) and newly developed molecular level liquid – liquid doping methods [16]. This motivated studies aiming to improve the fracture toughness of the Mo-Si-B alloys in this regime by doping with rare earth oxides (such as  $\text{La}_2\text{O}_3$ ), which led to an increase from  $\sim 5 \text{ MPa}\sqrt{\text{m}}$  to  $\sim 9 \text{ MPa}\sqrt{\text{m}}$  at ambient temperatures [17,18].

Alloys synthesized from regime (2) show superior high temperature strength and oxidation resistance due to the presence of the Si-rich T1 and the B-rich T2 phases. It was observed that the T1 has higher resistance to oxidation and higher temperature strength

<sup>\*</sup> Corresponding author.<sup>\*\*</sup> Corresponding author.E-mail addresses: [sk.makineni@mpie.de](mailto:sk.makineni@mpie.de) (S.K. Makineni), [b.gault@mpie.de](mailto:b.gault@mpie.de) (B. Gault).

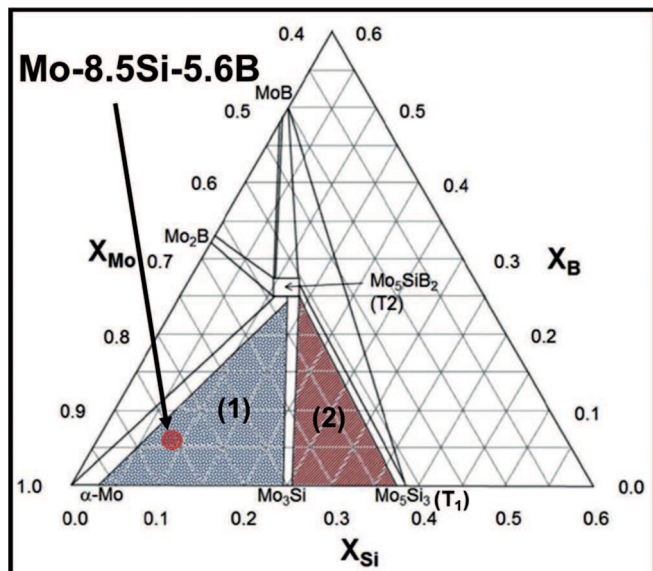


Fig. 1. Mo rich corner of Mo-Si-B phase diagram (1600 °C isotherm) adapted from Ref. [3] showing the Mo-3.1Si-0.8B (Mo-8.5Si-5.6B, in at.%) composition (measured by ICP analysis) in the phase regime of  $\alpha$ -Mo +  $\text{Mo}_3\text{Si}$  +  $\text{Mo}_5\text{SiB}_2$  (Berczik's triangle, [5,6]).

compared to the  $\text{Mo}_3\text{Si}$  phase [1,19,20]. These properties motivated several attempts to develop alloys based on the combination of the  $\alpha$ -Mo + T1 + T2 for yielding a material with a good combination of high-temperature mechanical and oxidation properties. Recent studies have shown that an addition of more than approx. 25 at.% amount of Ti, Nb and W stabilizes a phase combination of  $\alpha$ -Mo + T1 + T2, which led to creep properties superior to those of single-crystalline Ni-based superalloys [21–24]. However, these alloys showed inferior high temperature oxidation resistance [24,25].

The main synthesis and processing routes explored so far for making these Mo-Si-B based alloys are ingot solidification (arc melting) and powder processing (ball milling/atomization and consolidation). Application of additive manufacturing (AM) techniques has not been explored yet. Selective laser melting (SLM) has opened a wide range of new opportunities for the processing and fabrication of metallic products with complex constitutional design and shapes impossible to achieve via conventional wrought/casting and powder methods [26–28]. SLM involves the layer-by-layer fabrication, controlled through a computer aided design (CAD) software, of a metallic component through the successive local melting and solidification of typically pre-alloyed powders through the deposition of energy from a laser beam. This technology has been implemented successfully in producing a range of engineering alloys such as oxide-dispersion-strengthened steels [29] and high temperature nickel-based superalloys [30,31]. Recently, the feasibility of applying SLM to molybdenum with its high melting point of 2610 °C has been demonstrated [32,33].

In this context, we demonstrate in this study three main items: First, synthesis of Mo-Si-B based alloy by laser melting; Second, stabilization of a new phase regime containing the  $\alpha$ -Mo + T1 + T2 without using any additional alloying addition, and this phase regime is shown to be stable even after annealing at 1200 °C for 200 h; Third, we obtained rare earth oxides dispersion into the microstructure. Local individual phase properties such as hardness and elastic modulus have been evaluated using nano-indentation.

## 2. Experimental

### 2.1. Alloy formation by laser melting

Two batches of pure elemental powders of Mo (3–7  $\mu\text{m}$ ), Si (1–5  $\mu\text{m}$ ) and B (–325 mesh size), supplied by Sigma Aldrich, were mixed homogeneously in a laboratory scale ball milling unit (PULVERISETTE 7, FRITSCH, using 10 mm diameter tungsten carbide balls) for 10 h. One batch included 1 wt.%  $\text{La}_2\text{O}_3$  particles (particle size  $\sim 100$  nm). We chose the alloy composition Mo-4.2Si-1.1B (in wt.%; Mo-12Si-8B, in at. %) that falls into phase regime (1).

The milled powder mixture was subjected to laser heating for melting and alloy synthesis. The powder was placed in grooves milled into a 316/1.4404 stainless-steel substrate (see Fig. 2(a)) and subsequently exposed to the laser operated at 400 W power (Ytterbium fibre laser system, IPG Laser GmbH, with a wavelength of 1070 nm and a focus diameter of 1 mm). The laser speed was kept at 20 mm/s. These parameters were selected for melting a Mo-rich alloy with its high melting point, based on the estimation of the energy deposited by the laser beam (see supplementary information S1). The laser energy density is estimated to be around  $40 \text{ kJ cm}^{-3}$  which exceeds the energy density required to melt a Mo rich alloy ( $14 \text{ kJ cm}^{-3}$ ).

The process was iterated with 12 passes, manually adding a powder layer of approximate thickness of 0.5 mm each time, until a 5 mm-height sample was fabricated on the substrate. To minimize contamination from the substrate into the alloy, the first three layers were melted using pure-Mo powder. Cross-section samples of the alloy were cut using a diamond saw and were mechanically polished for characterization. A schematic diagram with an optical micrograph of the cross-section is shown in Fig. 2. The overall alloy composition was measured by inductively coupled plasma (ICP) analysis and found to be Mo-3.1Si-0.8B (in wt.%) with 0.8 wt.%  $\text{La}_2\text{O}_3$ .

### 2.2. X-ray diffraction (XRD)

Phase identification was carried out by X-ray diffraction using an ISO-DEBYEFLEX 3003 equipped with  $\text{Co K}_{\alpha 1}$  ( $\lambda = 1.788965 \text{ \AA}$ ) radiation as a source operated at 40 kV and 25 mA between 20 and 120 deg ( $2\theta$ ) at a step size ( $\Delta 2\theta$ ) of 0.03 deg and a counting time of 20 s per step. The X-ray beam shape was in point focus with a beam size of 0.7 mm.

### 2.3. Microstructural characterization

Scanning electron microscopy (SEM, ZEISS MERLIN) was used for imaging and phases were identified by using wavelength-dispersion spectroscopy (WDS) in an electron probe micro-analyzer (JEOL JXA-8100). Transmission electron microscopy (TEM) was carried out using a Phillips CM-20 instrument operated at 200 kV. The indexing and simulation of TEM diffraction patterns obtained from the evolved phases were carried out using the JEMS software [34].

Atomic-scale compositional analysis on the phases was done using atom probe tomography (APT). Samples for TEM and APT were fabricated using a dual beam SEM/focused-ion-beam instrument (FEI Helios Nanolab 600) in conjunction with an in-situ lift-out method. To remove regions severely damaged by the high-energy (30 kV) Ga ion beam during APT specimen and TEM lamellae fabrication, a final cleaning procedure was carried out at 2 kV and 16 pA current. APT measurements were conducted using a LEAP<sup>TM</sup> 3000X HR (Cameca Instruments), equipped with a reflectron lens. Laser pulsing mode (532 nm wavelength, 10 ps pulse duration,  $\sim 10 \mu\text{m}$  spot size) was applied at a pulse repetition rate of

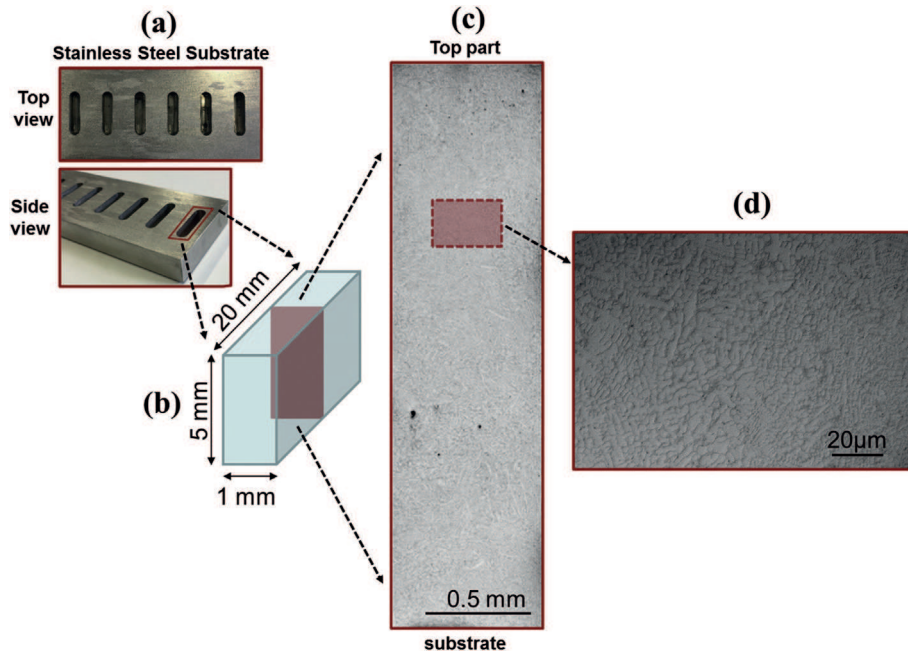


**Fig. 2.** (a) A stainless steel substrate top view and side view with grooves of depth 7 mm. (b) Schematic of the built-up laser melted alloy. Optical micrographs of (c) the entire cross-section and from (d) the marked region at higher magnification.

250 kHz and a pulse energy of 0.4 nJ. The specimen's base temperature was kept at 60 K and the target detection rate was set to be 5 ions detected every 1000 pulses. Data analysis was performed using the software package IVAS 3.6.14.

#### 2.4. Mechanical properties

The room temperature indentation fracture toughness was measured using Vickers diamond pyramid indentation, which is a well-established probing tool for similar brittle materials and applicable to small scale specimens [35–37]. A Hysitron TriboScope 950 nano-indenter system was used for nano-hardness testing. The system contained a XYZ sample stage and a setup which combines a piezo-scanner with a transducer. The nano-indentation was carried out using Berkovich diamond indenter. Indentation on individual phases was carried out in displacement controlled mode up to a 50 nm range with the loading and unloading rate being maintained at a value of 10 nm/s and the loading time was 5s. Load and displacement were measured simultaneously during indentation. Standard calibration was performed beforehand at various depths on quartz. For indentation fracture toughness calculation, indentations with a load of 1 kg were performed with a Vickers diamond pyramid indenter. To generate a large amount of indentation cracks in the microstructure, a load of 5 kg was also applied.

### 3. Results

#### 3.1. Identification of phases by X-ray diffraction (XRD)

Fig. 3(a) and (b) shows a comparison of XRD patterns for the ball milled (10 h) Mo-Si-B-La<sub>2</sub>O<sub>3</sub> powder and of the deposited specimen after laser melting. The as-milled powders show only  $\alpha$ -Mo diffraction peaks with a body centered cubic (bcc) crystal structure but neither peaks from B/Si nor any other intermetallics phases were detected. The measured lattice parameter of  $\alpha$ -Mo is 3.1362 Å.

After laser exposure, intermetallic phases emerge. XRD shows that  $\alpha$ -Mo solid solution, T1 and T2 phases have evolved. The T1 has

tetragonal crystal structure with space group I4/mcm and a lattice parameters of  $a = 9.6443$  Å and  $c = 4.9090$  Å, respectively. The boron rich T2 forms in D8<sub>1</sub> body-centered tetragonal crystal structure with the same space group I4/mcm but it has different lattice parameters with values  $a = 5.998$  Å and  $c = 11.027$  Å. Interestingly, this is not the combination of equilibrium phases expected for the alloy composition selected. The phase diagram in Fig. 1 suggests formation of Mo<sub>3</sub>Si instead of T1 along with the  $\alpha$ -Mo and T2. The  $\alpha$ -Mo lattice parameter was measured to be 3.1442 Å. The  $\alpha$ -Mo peaks become narrower and shift to the right after laser melting, as revealed by the inset that shows the comparison of the highest intensity [110]  $\alpha$ -Mo diffraction peak. This observation indicates a lattice expansion of  $\alpha$ -Mo after laser melting and solidification of the ball milled powder. This behavior is in accordance with reports by Krüger et al. [38] that the  $\alpha$ -Mo lattice tends to contract in Mo-Si and Mo-Si-B alloys, after around 10 h of ball milling. They attributed this observation to the dissolution of lower atomic radius Si/B solutes into the  $\alpha$ -Mo bcc lattice. Here, the lattice parameter of the  $\alpha$ -Mo phase is measured to be 3.1362 Å after 10 h of ball milling, lower than that of the pure Mo (lattice parameter of 3.14608 Å). This observation indicates supersaturation of the  $\alpha$ -Mo by Si and B solutes. After subsequent laser melting of the milled powder, the lattice parameter of the  $\alpha$ -Mo increases to 3.1442 Å and the intermetallic phases emerge. This lattice expansion of the  $\alpha$ -Mo suggests that the dissolved Si/B solutes were rejected from the  $\alpha$ -Mo and partitioned to form the respective phases T1 and T2 during rapid solidification of the laser melt pool. Importantly, Fig. 3(c) shows the XRD pattern after annealing at 1200 °C, 200 h for laser melted alloy. Peaks corresponding to  $\alpha$ -Mo, T1 and T2 were identified. This finding shows that the new phase combination is stable at 1200 °C for 200 h.

#### 3.2. Microstructural investigation of the laser melted alloys

The backscattered scanning electron (BSE) micrographs in Fig. 4(a) and (b) show the  $\alpha$ -Mo dendritic microstructures for laser melted Mo-Si-B alloy with and without La<sub>2</sub>O<sub>3</sub> particles respectively.



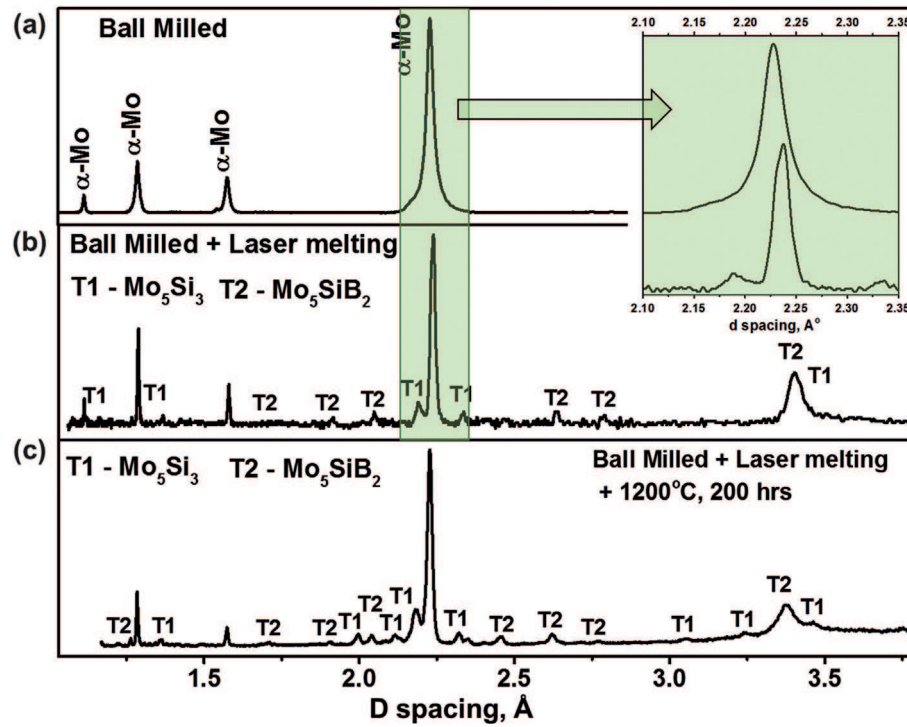


Fig. 3. Comparison of X-ray diffraction patterns obtained for a Mo-Si-B-LazO<sub>3</sub> alloy (a) after ball milling, (b) after laser melting and (c) subsequent annealing at 1200 °C for 200 h.

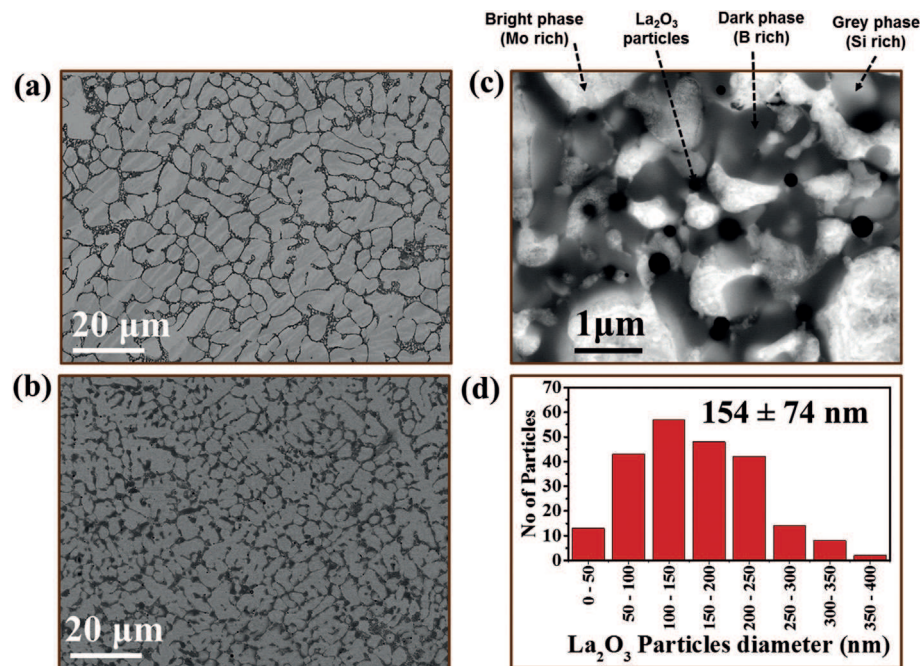


Fig. 4. Scanning electron micrographs for (a) the laser melted Mo-Si-B alloy without oxide particles, (b) the laser melted Mo-Si-B-LazO<sub>3</sub> alloy and (c) at high magnification showing inter-dendritic region with dark contrast phase (B rich), grey phase (Si rich) and the dark particles (La<sub>2</sub>O<sub>3</sub>) (d) Size distribution for the oxide La<sub>2</sub>O<sub>3</sub> particles in the alloy.

The microstructure is clearly coarser in the alloy without oxide particles. Fig. 4(c) shows a higher magnification BSE image of an inter-dendritic region for the alloy with oxide particles. The phases exhibits different contrast depending on their relative average atomic number. WDS spot analysis (see Supplementary Table S2) enabled us to determine that the bright phase is the  $\alpha$ -Mo solid solution, the dark grey and light grey phases in the inter-dendritic

regions are B-rich and Si-rich phases, respectively. The area fractions of these phases in the microstructure are measured to be ~70%, 21% and 9%, respectively. The compositions obtained by WDS are taken qualitatively in order to distinguish the phases due to the limitation posed by the overlap of the interaction volumes.

Additionally, there is a clear contrast between the three phases and the dark particles embedded mostly in the inter-dendritic

regions. These dark particles appear similar to pores found in many alloys synthesized through laser additive manufacturing. Alternatively, when considering the drastic change in the morphology of the phases, it is also possible that these dark zones are the dispersed  $\text{La}_2\text{O}_3$  particles. It was subsequently confirmed through atom probe tomography that these particles are indeed lanthanum and oxygen rich particles (see section 3.4). The size distribution of the  $\text{La}_2\text{O}_3$  particles is shown in Fig. 4(d) with an average diameter of  $154 \pm 74$  nm. Unlike previous studies on similar alloys fabricated from conventional sintering processes [17,18], the  $\text{La}_2\text{O}_3$  particles are found mostly in the inter-dendritic regions where the two intermetallic phases are also present, and not in the  $\alpha$ -Mo. In addition, we could not observe any solidification cracks throughout the cross-section of the sample as otherwise pure Mo, with its high melting point, is susceptible to crack formation during SLM [32,33].

### 3.3. Crystallographic analysis of the phases by transmission electron microscopy (TEM)

The existence and crystal structures of the  $\alpha$ -Mo, as well as of the T1 and T2 phases were further analyzed and confirmed by TEM. Fig. 5(a) shows a bright field image taken near to the inter-dendritic region of the laser melted oxide-dispersed Mo-Si-B alloy. The diffraction patterns taken from the dendrite, indexed in terms of  $\alpha$ -Mo with a bcc crystal structure, suggest a growth direction aligned near to the  $[313]$  zone axis. In Fig. 5(a), a phase near the dendrite exhibits darker contrast and the diffraction pattern taken from this region indicates that it has the structure of the boron-rich T2 phase aligned near to the  $[\bar{7}21]$  zone axis. The combined indexed diffraction patterns taken from the interface (red circle) among the  $\alpha$ -Mo and T2 phases are also shown in Fig. 5(b) along with the simulated and indexed schematic patterns. From the stereographic projection (see Supplementary Fig. S3 for overlapped stereograms), we found that these phases tend to align with the following orientation relationship

$$[00\bar{1}]_{\alpha\text{Mo}} \parallel [\bar{1}\bar{1}\bar{1}]_{\text{Mo}_5\text{SiB}_2(\text{T2})}$$

$$(\bar{0}20)_{\alpha\text{Mo}} \parallel (312)_{\text{Mo}_5\text{SiB}_2(\text{T2})}$$

which agrees with observations mentioned in Ref. [39]. Respective

dark field images taken from  $(\bar{2}02)$  and  $(02\bar{4})$  diffraction spots, corresponding to the  $\alpha$ -Mo and T2 phases respectively, are also shown (Fig. 5(c)). Similarly, we found another phase with darker contrast when the foil is oriented near to the  $[313]$  zone of the same  $\alpha$ -Mo dendrite, as shown in Fig. 6(a).

The indexing of the diffraction pattern from the darker contrast region reveals that the region contains a Si-rich T1 phase aligned near to the  $[312]$  zone axis. The combined pattern obtained from the interface region (red circle) between the  $\alpha$ -Mo and the Si-rich T1 phase is also shown in Fig. 6(b) along with the corresponding simulated and indexed schematic patterns. From the stereographic projection analysis (See Supplementary Fig. S4 for overlapped stereograms), we deduce an unreported orientation relationship of:

$$[\bar{2}\bar{1}\bar{3}]_{\alpha\text{Mo}} \parallel [\bar{1}\bar{1}0]_{\text{Mo}_5\text{Si}_3(\text{T1})}$$

$$(\bar{2}\bar{1}1)_{\alpha\text{Mo}} \parallel (\bar{1}14)_{\text{Mo}_5\text{Si}_3(\text{T1})}$$

A dark field micrograph taken from the  $(1\bar{3}0)$  diffraction spot corresponding to the T1 is also shown in Fig. 6(c).

### 3.4. Compositional analysis of the phases by atom probe tomography (APT)

Precise compositional measurements were obtained from APT, as summarized in Fig. 7(a–b) where an APT reconstruction of a specimen containing all three phases is shown. An iso-composition surface that delineates regions containing above 19 at.% B highlights the location of the different phases. The composition profiles across interface 1 is shown in Fig. 7(b).

The composition measured, after background correction, of the silicon rich phase is 62.6 at.% Mo – 37.1 at.% Si – 0.2 at.% B, which accurately matches the stoichiometry  $\text{Mo}_5\text{Si}_3$  of the intermetallic T1. Similarly the measured composition of the boron rich phase is 63.1 at.% Mo – 12.7 at.% Si – 24.2 at.% B, which is near the  $\text{Mo}_5\text{SiB}_2$  stoichiometry of the intermetallic T2. The  $\alpha$ -Mo composition was measured on another set of specimens that were prepared from site-specific lift-out tips taken from the regions near to the center of the dendrites. The Supplementary Fig. S5 shows an example of an APT reconstruction from the  $\alpha$ -Mo dendrite revealing the

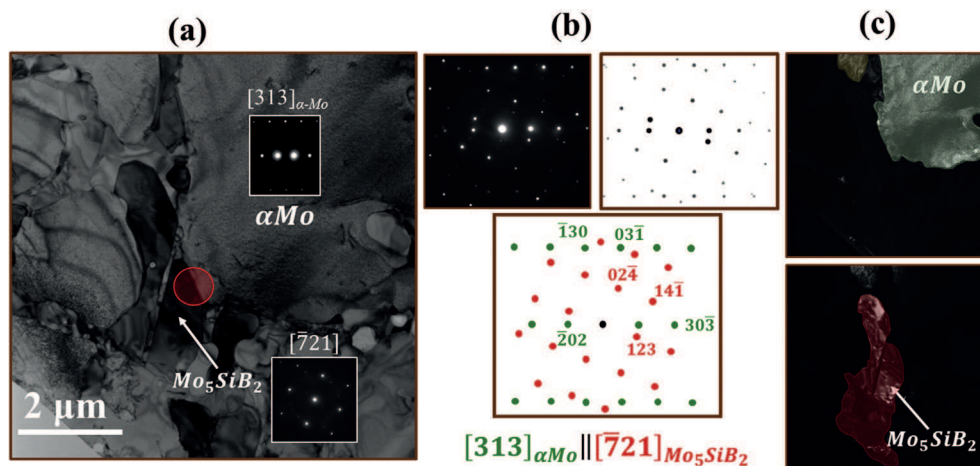


**Fig. 5.** (a) Bright field micrographs taken along the  $[313]$   $\alpha$ -Mo zone axis revealing the orientation relationship of the matrix with  $\text{Mo}_5\text{SiB}_2$  (T2). (b) Diffraction pattern taken from the interface region (red circle) in (a) with their simulated and schematic indexed pattern: in green is  $\alpha$ -Mo, in red is the  $\text{Mo}_5\text{SiB}_2$  phase; (c) Dark field micrographs taken using  $(\bar{2}02)$   $\alpha$ -Mo, the phase highlighted in green color is reflected, and using the  $(024)$   $\text{Mo}_5\text{SiB}_2$  spot, the phase highlighted in red is reflected. (For interpretation of the references to color in this figure legend, the reader is referred to the Web version of this article.)

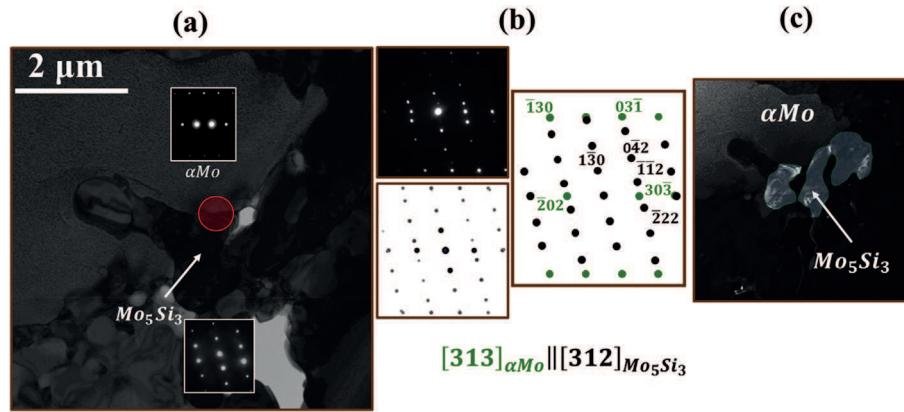


**Fig. 6.** (a) Bright field micrographs taken along the  $[313]$   $\alpha\text{-Mo}$  zone axis revealing the orientation relationship of the matrix with  $\text{Mo}_5\text{Si}_3$ . (c) Diffraction pattern taken from the interface region (red circle) in (a) with their simulated and schematic indexed pattern: in green spots is the  $\alpha\text{-Mo}$  and in black the  $\text{Mo}_5\text{Si}_3$  phase. (c) Dark field micrograph using the  $(1\bar{3}0)$   $\text{Mo}_5\text{Si}_3$  reflection highlighted in blue. (For interpretation of the references to color in this figure legend, the reader is referred to the Web version of this article.)

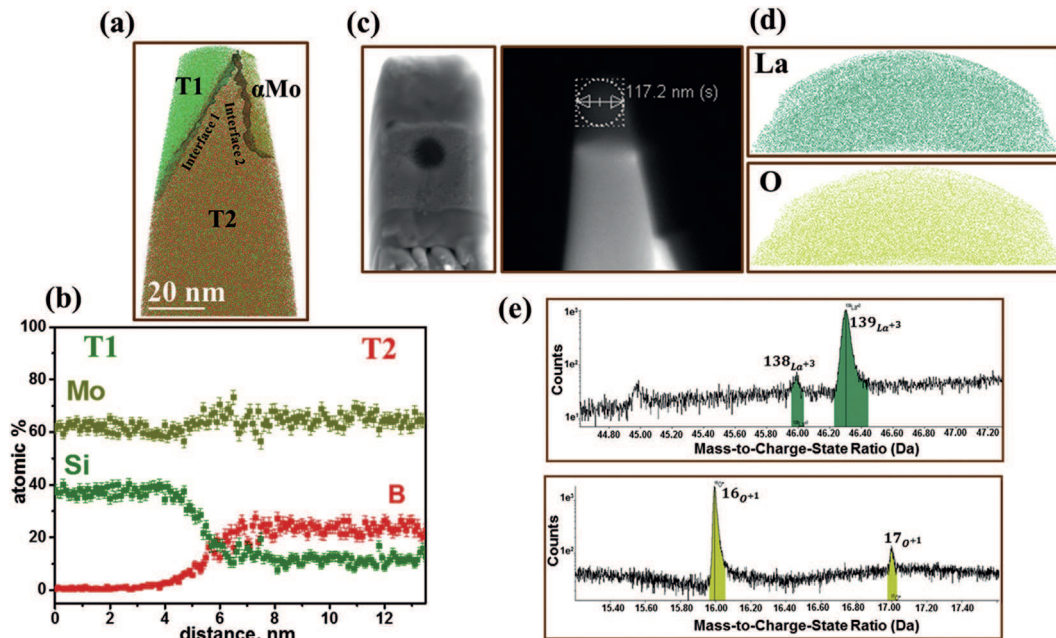


**Fig. 7.** (a) Atom probe tomography reconstruction of an Mo-Si-B alloy tip containing all three phases separated by interfaces 1 and 2 with  $\text{Mo}_5\text{Si}_3/\text{Mo}_5\text{SiB}_2$  and  $\text{Mo}_5\text{SiB}_2/\alpha\text{-Mo}$  respectively. (b) Elemental composition profile across interface 1. (c) Site specific lift out of a specimen around the dark particle present in the microstructure of the Mo-Si-B alloy containing oxide particles. SEM micrographs showing presence of dark particle in the cut section of the APT lamella and the APT tip with the particle. (d) APT reconstruction of the tip revealing the Lanthanum and Oxygen atoms. (e) Mass spectrum of the tip showing the peaks from Lanthanum and Oxygen.

distribution of Mo, Si and B. The composition was found to be Mo – 2.04 at.% Si with no measurable B content after background correction.

For the oxide particles appearing in dark contrast, specimens for APT were prepared by site-specific lift-out, to leave a particle exactly at the tip of the needle-shaped specimen, as depicted in Fig. 7(c). The obtained reconstructions and mass spectra shown from these analyses are shown in Fig. 7(d) and (e) respectively. The composition of the particle was measured as 38.7 at.% La + 61.3 at.% O, which is as close to the  $\text{La}_2\text{O}_3$  stoichiometry as can be expected from APT measurements which are known to have issues with O composition measurements in oxides [40–42].

### 3.5. Mechanical properties

#### 3.5.1. Evaluation of hardness and modulus of respective phases by nano-indentation

For identifying the respective mechanical properties of individual phases in this new multi-phase regime, nano-indentation was performed. Fig. 8(a–c) shows the representative load displacement curves obtained for the three phases present in the microstructure. The nano-indentation data was analyzed using the Oliver and Pharr method [43]. The measured hardness and modulus values for the phases are shown in Fig. 8(d). A significant difference in both values was observed among the three phases.



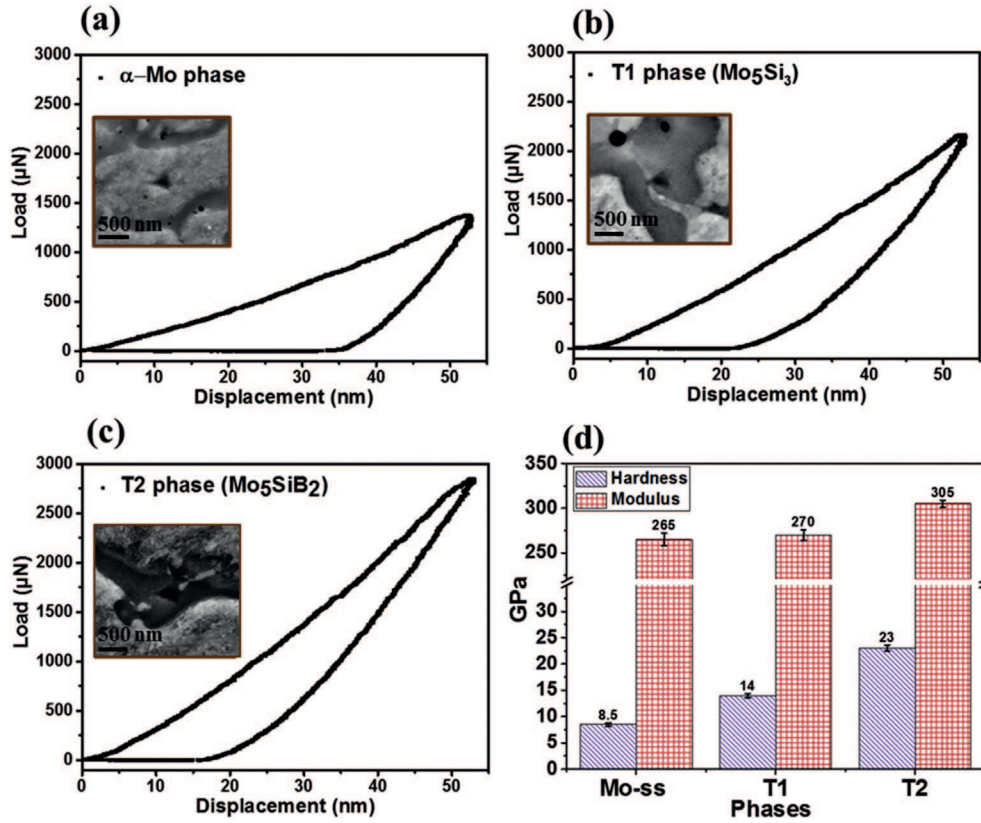


Fig. 8. Representative Load displacement curves obtained from nano-indentation on individual phases of (a)  $\alpha$ -Mo (b)  $\text{Mo}_5\text{Si}_3$  (T1) and (c)  $\text{Mo}_5\text{SiB}_2$  (T2) and their corresponding representative SEM images as insets respectively. (d) Comparison of average hardness and reduced elastic modulus of all the three phases.

The  $\alpha$ -Mo phase shows an average hardness value of  $8.5 \pm 0.3$  GPa with a reduced elastic modulus of  $265 \pm 7$  GPa. The hardness of the  $\alpha$ -Mo phase is similar to the values obtained in conventionally cast Mo-Si-B alloys [44,45]. For the T2 phase, the obtained hardness and modulus values are  $23 \pm 0.6$  GPa and  $305 \pm 4$  GPa while for the T1 phase, the values are  $14 \pm 0.4$  GPa and  $270 \pm 6$  GPa, respectively, falling in-between the values obtained for  $\alpha$ -Mo and T2. From the measured reduced modulus ( $E_r$ ) for each phase, we have calculated the respective elastic modulus ( $E$ ) using the standard relation [46].

$$\frac{1}{E_r} = \frac{1 - \nu^2}{E} + \frac{(1 - \nu^2)}{E_i}$$

(where  $i$  stands for indenter i.e. Berkovich diamond indenter; ' $\nu$ ' denotes Poisson's ratio).

The calculated elastic moduli ( $E$ ) for the  $\alpha$ -Mo, T1 and T2 have average values of 305, 312 and 367 GPa, respectively, when assuming a Poisson's ratio ( $\nu$ ) of 0.3 for each of the Mo-rich phases. For the  $\alpha$ -Mo solid solution, Yang et al. [47] reported an elastic modulus of 310 GPa with a Si content of  $\sim 2.6$  at.%. In the present laser melted alloy, the  $\alpha$ -Mo phase contains  $\sim 2.05$  at.% Si and shows an elastic modulus of  $305 \pm 7$  GPa, which is in the same range. For T1 and T2, the reported elastic moduli are 323 GPa and 383 GPa for bulk samples [48], slightly higher than the values determined in the present alloy by nano-indentation. This can be attributed to unavoidable superposition with nearby interphase boundaries in our measurements. The calculated values of elastic moduli for the phases obtained in the current microstructure were used as one of the inputs to evaluate the indentation fracture toughness in the next section.

### 3.5.2. Estimation of micro-indentation fracture toughness

The indentation fracture toughness was evaluated for the laser melted Mo-Si-B alloy both with and without  $\text{La}_2\text{O}_3$  particles, so as to identify the effect of the incorporation of the oxide particles. We assessed the fracture toughness by micro-indentation measurements with a 1 kg load owing to the limited amount of synthesized material available. At least 12 indents were made to derive an average value.

Fig. 9(a) shows a representative low magnification image of one of the indent impressions on the surface of the oxide dispersed Mo-Si-B alloy. A higher magnification image (Fig. 9(b)) reveals, at one of the corner of the indent impression, the formation of a crack and its interaction/deflection (out of plane) with the oxide particle and subsequent crack trapping at ductile  $\alpha$ -Mo phase. The indentation fracture toughness ( $K_i$ ) was evaluated by using the Lankford criterion [34] suited for non-ductile materials

$$K_i = 0.0782 \left( H_v a^{0.5} \right) (E/H_v)^{0.4} (c/a)^{-1.56}$$

Where,  $c$  is the post indentation crack length,  $a$  is the indentation dimension,  $H_v$  is the Vickers hardness number and  $E$  is the elastic modulus that has been predicted for this multi-phase alloy using the linear rule of mixture from the values of the individual phases as determined by nano-indentation. The weights assigned to the individual phase portions in the rule of mixture proportionally to their volume fractions determined from electron micrographs (see 3.2). The volume fraction of the oxide particles was not taken into account since these will contribute to the toughness of the alloy through an extrinsic mechanism. The resultant weighted average elastic modulus ( $E$ ) was estimated to be  $\sim 313$  GPa by using the estimated values of 305 GPa, 312 GPa and 367 GPa for  $\alpha$ -Mo, T1 and

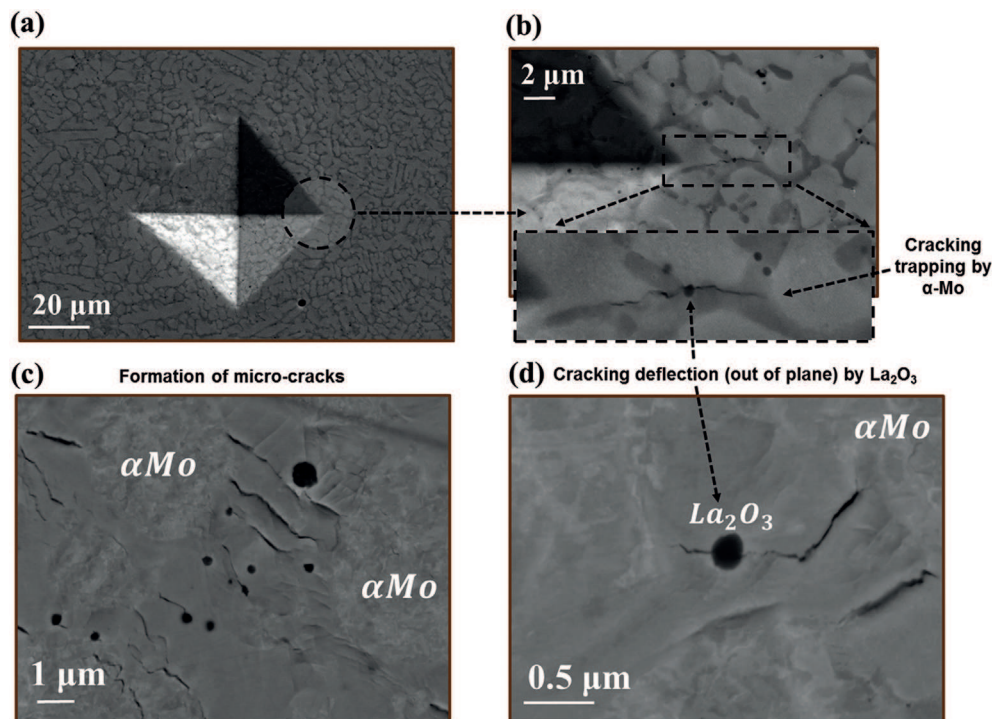


**Fig. 9.** SEM micrographs for Mo-Si-B-La<sub>2</sub>O<sub>3</sub> alloy showing (a) an indent with 1 kg load and (b) crack propagation from one of the indent corners and its interaction (deflection) due to the oxide particle (an extrinsic toughening mechanism) and its subsequent trapping in ductile  $\alpha$ -Mo phase, an intrinsic toughening mechanism. Macro indentation with 5 kg load: (c) Formation of micro-cracks mainly in inter-dendritic intermetallics region in the vicinity of La<sub>2</sub>O<sub>3</sub> particles and (d) as an example of micro-crack deflection by a La<sub>2</sub>O<sub>3</sub> particle providing extrinsic toughening to the alloy.

T2 respectively as obtained from nano-indentation. The measured  $c/a$  and  $H_v$  values are  $\sim 1.05$  and  $\sim 690$  VHN. With this input, the average indentation fracture toughness was calculated to be  $\sim 18$  MPa $\sqrt{m}$ . For the Mo-Si-B alloy without the oxide particles, a lower average value of  $\sim 12$  MPa $\sqrt{m}$  was measured.

Further, to generate a large number of cracks, the laser melted alloy were indented using a Berkovich pyramidal tip with a higher load of 5 kg. The micrographs in Fig. 9(c–d) (see also Supplementary Fig. S6) show formation of micro-cracks mostly in the intermetallic phase region in the vicinity of oxide particles, and the micro-cracks were trapped in the ductile  $\alpha$ -Mo phase, finally, micro-crack deflections were also observed (as shown in Fig. 9(d)), contributing to the fracture toughness extrinsically [11].

#### 4. Discussion

Our work advances the field of Mo-Si-B based alloys mainly in two ways: first, we synthesized the material by additive manufacturing, which allowed us to exploit the rapid quenching to reach a regime of multiple non-equilibrium phases ( $\alpha$ -Mo, T1, T2) not obtained so far through conventional synthesis and processing routes. This phase regime remains stable even after annealing for 200 h at 1200 °C. Second, we show the possibility of modifying the alloy by oxide particle dispersion that leads to an improvement in indentation fracture toughness.

The measured bulk composition of Mo-3.1Si-0.8B falls in the phase regime of  $\alpha$ -Mo + Mo<sub>3</sub>Si + T2, however, in the present case, we observe the suppression of Mo<sub>3</sub>Si phase and formation of the T1 phase. The combined structural (XRD, TEM) and compositional (APT) results confirmed the formation, structure and composition of each phase. The  $\alpha$ -Mo matrix forms primary dendrites with a phase fraction of  $\sim 70\%$ . T1 and T2 form in the inter-dendritic regions with phase fractions of  $\sim 21\%$  and  $9\%$ , respectively. This new

phase regime is attributed to the fast cooling rate during solidification. In laser-based additive manufacturing, typical cooling rates are of the order of  $10^3$ – $10^6$  Ks<sup>−1</sup>, i.e. much higher than in conventional casting with  $\sim 10^1$ – $10^2$  Ks<sup>−1</sup>, as the small melt pool cools down very rapidly due to high heat conduction from the molten pool into the cold substrate. In the Mo-Si-B alloy system, the phase melting points are  $\alpha$ -Mo (2610 °C) > Mo<sub>5</sub>SiB<sub>2</sub> (T2, 2200 °C) > Mo<sub>5</sub>Si<sub>3</sub> (T1, 2180 °C) > Mo<sub>3</sub>Si (2022 °C) [11]. Hence, it seems likely that the undercooling offered by laser melting may promote the observed suppression of the equilibrium Mo<sub>3</sub>Si phase. Similar observations have been reported for previously studied Mo-Si-B based alloys [39], i.e. showing suppression of undesired and deleterious borides such as MoB and the Mo<sub>3</sub>Si phase with rapid solidification processing (RSP) by splat quenching (cooling rate  $\sim 10^7$  Ks<sup>−1</sup>) in a two phase  $\alpha$ -Mo + T2 alloy.

The microstructural observations suggest that during solidification after laser melting of the alloy, the  $\alpha$ -Mo solidifies first due to its higher melting point of 2600 °C in the form of primary dendrites. The dendrites reject the solute (Si and B) across the solid/liquid interface into the supercooled liquid and thus the liquid becomes enriched in Si and B. Subsequently, this solute enriched supercooled liquid solidifies at a very high solidification rate, thereby suppressing the equilibrium phase with the lowest melting point, i.e. Mo<sub>3</sub>Si, in the solidified microstructure. The inter-dendritic region finally contains only T1 and T2 solidified with specific orientations relative to the  $\alpha$ -Mo dendrite. This observation indicates non-equilibrium solidification due to the high cooling rate. In Fig. 4(a) and c, we show that the Mo-Si-B alloy, when doped with La<sub>2</sub>O<sub>3</sub> particles, has a much finer and continuous distribution of  $\alpha$ -Mo dendrites compared to the reference alloy without oxide. This can be attributed due to a grain-refining effect of the oxide particles that provide nucleation sites for  $\alpha$ -Mo dendrites during solidification.



In the present oxide dispersed Mo-Si-B alloy, both intrinsic and extrinsic mechanisms contribute to improving the indentation fracture toughness. Intrinsic toughening occurs ahead of the crack tip while extrinsic toughening occurs in the wake of the crack tip known as “shielding” of the crack. The finer microstructure in the oxide-dispersed alloy likely explains the improved fracture toughness values at room temperature: a continuously arranged and compliant  $\alpha$ -Mo matrix morphology forms that enables blunting/trapping of crack tips which is an intrinsic mechanism contributing towards toughness [49,50]. Additionally, oxide particles in the brittle intermetallic regions tend to induce micro-cracks in the vicinity of them (Fig. 9(c)) and thus generate new surfaces that absorb higher energy, which contributes to an improved fracture toughness [49,50]. Further, we observe that these micro-cracks were deflected by the oxide particles (Fig. 9(b–d)) in the intermetallic phase region, which can provide additional extrinsic toughening to the alloy at room temperature. All these factors contribute to the comparatively high indentation fracture toughness of the oxide containing alloy which marks a progress of ~33% compared to the value of ~12 MPa $\sqrt{m}$  observed for the Mo-Si-B reference alloy without oxide dispersion. Kruzic et al. [14] showed that the presence of even a 49 vol% fraction ductile  $\alpha$ -Mo with continuously arranged morphology, produced by the method described in Ref. [15], can lead to a fracture toughness of up to 20 MPa $\sqrt{m}$  in higher Si/B content Mo-7.6Si-1.5B (Mo-20 at.%Si-10 at.%B) materials which otherwise have ~5 MPa $\sqrt{m}$  fracture toughness values when fabricated by conventional powder processing methods. The present Mo rich Mo-3.1Si-0.8B (Mo-8.5 at.%Si-5.6 at.%B) alloy has a higher ductile  $\alpha$ -Mo volume fraction (70%) with homogeneous topological distribution. When blended with oxides in fine dispersion the Mo-Si-B alloy contains an additional extrinsic toughening feature conveying an indentation fracture toughness value of ~18 MPa $\sqrt{m}$  to the material.

## 5. Conclusions

- 1) We demonstrate the fabrication of dense Mo-Si-B-based alloys through an additive laser melting technique that results in a typical dendritic solidified alloy microstructure. No additional high temperature sintering methods were required.
- 2) We show existence of a microstructure with a previously undocumented phase regime comprising  $\alpha$ -Mo dendrites with Mo<sub>5</sub>Si<sub>3</sub> (T1) and Mo<sub>5</sub>SiB<sub>2</sub> (T2) phases in the inter-dendritic regions of the laser melted alloys. The obtained phase regime is found to be stable even after annealing at 1200 °C for 200 h.
- 3) Oxide particles (such as La<sub>2</sub>O<sub>3</sub> in the present case) were successfully dispersed in the microstructure and were observed to arrange mainly in the inter-dendritic phase regions, resulting in a refined microstructure and enhanced indentation fracture toughness.
- 4) The indentation fracture toughness value was calculated to be ~18 MPa $\sqrt{m}$  for the alloy variant with La<sub>2</sub>O<sub>3</sub> particles. The toughening is attributed to crack trapping (intrinsic toughening mechanism) by the presence of continuously distributed ductile  $\alpha$ -Mo phase in the microstructure and additional extrinsic toughening from oxide particles by formation of micro-cracks and crack deflection.

## Acknowledgements

The authors are grateful to U. Tezins and A. Sturm for their technical support of the atom probe tomography and focus ion beam facilities at the Max-Planck-Institut für Eisenforschung. The authors would like to acknowledge J. Wichert for ball milling and Laser melting operation, B. Breitbach for X-ray analysis and I.

Wossack for WDS measurements. SKM acknowledges financial support from the Alexander von Humboldt Foundation and DFG SFB TR 103.

## Appendix A. Supplementary data

Supplementary data related to this article can be found at <https://doi.org/10.1016/j.actamat.2018.03.037>.

## References

- [1] M. Meyer, M. Kramer, M. Akinc, Boron-doped molybdenum silicides, *Adv. Mater.* 8 (1996) 85–88, <https://doi.org/10.1002/adma.19960080118>.
- [2] J.H. Perepezko, The hotter the engine, the better, *Science* 326 (2009) 1068–1069, <https://doi.org/10.1126/science.1179327>.
- [3] J.A. Lemberg, R.O. Ritchie, Mo-Si-B alloys for ultrahigh-temperature structural applications, *Adv. Mater.* 24 (2012) 3445–3480, <https://doi.org/10.1002/adma.201200764>.
- [4] A.P. Alur, N. Chollacoop, K.S. Kumar, High-temperature compression behavior of Mo-Si-B alloys, *Acta Mater.* 52 (2004) 5571–5587, <https://doi.org/10.1016/j.actamat.2004.08.035>.
- [5] D.M. Berczik, Method for Enhancing the Oxidation Resistance of a Molybdenum Alloy, and a Method of Making a Molybdenum Alloy, 1997, US5595616 A, <http://www.google.com/patents/US5595616>. (Accessed 11 May 2017).
- [6] D.M. Berczik, Oxidation Resistant Molybdenum Alloy, 1995, <https://patents.google.com/patent/US5693156A/en>. (Accessed 27 January 2018).
- [7] V. Supatarawanich, D.R. Johnson, C.T. Liu, Effects of microstructure on the oxidation behavior of multiphase Mo-Si-B alloys, *Mater. Sci. Eng., A* 344 (2003) 328–339, [https://doi.org/10.1016/S0921-5093\(02\)00446-X](https://doi.org/10.1016/S0921-5093(02)00446-X).
- [8] J.H. Schneibel, C.T. Liu, L. Heatherly, M.J. Kramer, Assessment of processing routes and strength of a 3-phase molybdenum boron silicide (Mo<sub>5</sub>Si<sub>3</sub>-Mo<sub>5</sub>SiB<sub>2</sub>-Mo<sub>3</sub>Si), *Scripta Mater.* 38 (1998) 1169–1176, [https://doi.org/10.1016/S1359-6462\(97\)00558-7](https://doi.org/10.1016/S1359-6462(97)00558-7).
- [9] J.H. Schneibel, C.T. Liu, D.S. Easton, C.A. Carmichael, Microstructure and mechanical properties of Mo-Mo<sub>3</sub>Si-Mo<sub>5</sub>SiB<sub>2</sub> silicides, *Mater. Sci. Eng., A* 261 (1999) 78–83, [https://doi.org/10.1016/S0921-5093\(98\)01051-X](https://doi.org/10.1016/S0921-5093(98)01051-X).
- [10] P. Jain, K.S. Kumar, Tensile creep of Mo-Si-B alloys, *Acta Mater.* 58 (2010) 2124–2142, <https://doi.org/10.1016/j.actamat.2009.11.054>.
- [11] H. Choe, D. Chen, J.H. Schneibel, R.O. Ritchie, Ambient to high temperature fracture toughness and fatigue-crack propagation behavior in a Mo-12Si-8.5B (at.%) intermetallic, *Intermetallics* 9 (2001) 319–329, [https://doi.org/10.1016/S0966-9795\(01\)00008-5](https://doi.org/10.1016/S0966-9795(01)00008-5).
- [12] A.P. Alur, N. Chollacoop, K.S. Kumar, Creep effects on crack growth in a Mo-Si-B alloy, *Acta Mater.* 55 (2007) 961–974, <https://doi.org/10.1016/j.actamat.2006.09.028>.
- [13] P. Jain, K.S. Kumar, Dissolved Si in Mo and its effects on the properties of Mo-Si-B alloys, *Scripta Mater.* 62 (2010) 1–4, <https://doi.org/10.1016/j.scriptamat.2009.09.008>.
- [14] J.J. Kruzic, J.H. Schneibel, R.O. Ritchie, Ambient- to elevated-temperature fracture and fatigue properties of Mo-Si-B alloys: role of microstructure, *Metall. Mater. Trans.* 36 (2005) 2393–2402, <https://doi.org/10.1007/s11661-005-0112-5>.
- [15] J.H. Schneibel, M.J. Kramer, D.S. Easton, A Mo-Si-B intermetallic alloy with a continuous  $\alpha$ -Mo matrix, *Scripta Mater.* 46 (2002) 217–221, [https://doi.org/10.1016/S1359-6462\(01\)01227-1](https://doi.org/10.1016/S1359-6462(01)01227-1).
- [16] G. Liu, G.J. Zhang, F. Jiang, X.D. Ding, Y.J. Sun, J. Sun, E. Ma, Nanostructured high-strength molybdenum alloys with unprecedented tensile ductility, *Nat. Mater.* 12 (2013) 344–350, <https://doi.org/10.1038/nmat3544>.
- [17] Z. Guo-jun, D. Qian, K. Hao, W. Rui-hong, L. Gang, S. Jun, Microstructure and mechanical properties of lanthanum oxide-doped Mo-12Si-8.5B(at%) alloys, *J. Alloy. Comp.* 577 (Supplement 1) (2013) S493–S498, <https://doi.org/10.1016/j.jallcom.2012.03.037>.
- [18] W. Li, G. Zhang, S. Wang, B. Li, J. Sun, Ductility of Mo-12Si-8.5B alloys doped with lanthanum oxide by the liquid-liquid doping method, *J. Alloy. Comp.* 642 (2015) 34–39, <https://doi.org/10.1016/j.jallcom.2015.04.047>.
- [19] M.K. Meyer, M.J. Kramer, M. Akinc, Compressive creep behavior of Mo<sub>5</sub>Si<sub>3</sub> with the addition of boron, *Intermetallics* 4 (1996) 273–281, [https://doi.org/10.1016/0966-9795\(95\)00048-8](https://doi.org/10.1016/0966-9795(95)00048-8).
- [20] I. Rosales, H. Martinez, D. Bahena, J.A. Ruiz, R. Guardian, J. Colin, Oxidation performance of Mo<sub>3</sub>Si with Al additions, *Corrosion Sci.* 51 (2009) 534–538, <https://doi.org/10.1016/j.corsci.2008.12.004>.
- [21] R. Sakidja, J. Myers, S. Kim, J.H. Perepezko, The effect of refractory metal substitution on the stability of Mo(ss) + T2 two-phase field in the Mo-Si-B system, *Int. J. Refract. Metals Hard Mater.* 18 (2000) 193–204, [https://doi.org/10.1016/S0263-4368\(00\)00030-5](https://doi.org/10.1016/S0263-4368(00)00030-5).
- [22] P.K. Ray, Y.Y. Ye, M. Akinc, M.J. Kramer, Effect of Nb and W substitutions on the stability of the A15 Mo<sub>3</sub>Si phase, *J. Alloy. Comp.* 537 (2012) 65–70, <https://doi.org/10.1016/j.jallcom.2012.04.109>.
- [23] Y. Yang, H. Bei, S. Chen, E.P. George, J. Tiley, Y.A. Chang, Effects of Ti, Zr, and Hf on the phase stability of Mo<sub>ss</sub> + Mo<sub>3</sub>Si + Mo<sub>5</sub>SiB<sub>2</sub> alloys at 1600 °C, *Acta Mater.* 58 (2010) 541–548, <https://doi.org/10.1016/j.actamat.2009.09.032>.

- [24] D. Schliephake, M. Azim, K. von Klinski-Wetzel, B. Gorr, H.-J. Christ, H. Bei, E.P. George, M. Heilmaier, High-temperature creep and oxidation behavior of Mo-Si-B alloys with high Ti contents, *Metall. Mater. Trans.* 45 (2014) 1102–1111, <https://doi.org/10.1007/s11661-013-1944-z>.
- [25] Y. Liu, M.J. Kramer, A.J. Thom, M. Akinc, Oxidation behavior of multiphase Nb-Mo-Si-B intermetallics, *Metall. Mater. Trans.* 36 (2005) 601–607, <https://doi.org/10.1007/s11661-005-0175-3>.
- [26] W.E. Frazier, Metal additive manufacturing: a review, *J. Mater. Eng. Perform.* 23 (2014) 1917–1928, <https://doi.org/10.1007/s11665-014-0958-z>.
- [27] S.S. Babu, L. Love, R. Dehoff, W. Peter, T.R. Watkins, S. Pannala, Additive manufacturing of materials: opportunities and challenges, *MRS Bull.* 40 (2015) 1154–1161, [http://journals.cambridge.org/article\\_S0883769415002341](http://journals.cambridge.org/article_S0883769415002341). (Accessed 3 June 2017).
- [28] J.J. Lewandowski, M. Seifi, Metal additive manufacturing: a review of mechanical properties, *Annu. Rev. Mater. Res.* 46 (2016) 151–186, <https://doi.org/10.1146/annurev-matsci-070115-032024>.
- [29] Y.M. Wang, T. Voisin, J.T. McKeown, J. Ye, N.P. Calta, Z. Li, Z. Zeng, Y. Zhang, W. Chen, T.T. Roehling, R.T. Ott, M.K. Santala, P.J. Depond, M.J. Matthews, A.V. Hamza, T. Zhu, Additively manufactured hierarchical stainless steels with high strength and ductility, *Nat. Mater.* (2017), <https://doi.org/10.1038/nmat5021>.
- [30] K.A. Mumtaz, P. Erasenthiran, N. Hopkinson, High density selective laser melting of Waspaloy®, *J. Mater. Process. Technol.* 195 (2008) 77–87, <https://doi.org/10.1016/j.jmatprotec.2007.04.117>.
- [31] Q. Jia, D. Gu, Selective laser melting additive manufacturing of Inconel 718 superalloy parts: densification, microstructure and properties, *J. Alloy. Comp.* 585 (2014) 713–721, <https://doi.org/10.1016/j.jallcom.2013.09.171>.
- [32] D. Wang, C. Yu, J. Ma, W. Liu, Z. Shen, Densification and crack suppression in selective laser melting of pure molybdenum, *Mater. Des.* 129 (2017) 44–52, <https://doi.org/10.1016/j.matdes.2017.04.094>.
- [33] D. Faidel, D. Jonas, G. Natour, W. Behr, Investigation of the selective laser melting process with molybdenum powder, *Addit. Manuf.* 8 (2015) 88–94, <https://doi.org/10.1016/j.addma.2015.09.002>.
- [34] P.A. Stadelmann, EMS - a software package for electron diffraction analysis and HREM image simulation in materials science, *Ultramicroscopy* 21 (1987) 131–145, [https://doi.org/10.1016/0304-3991\(87\)90080-5](https://doi.org/10.1016/0304-3991(87)90080-5).
- [35] J. Lankford, Indentation microfracture in the Palmqvist crack regime: implications for fracture toughness evaluation by the indentation method, *J. Mater. Sci. Lett.* 1 (1982) 493–495, <https://doi.org/10.1007/BF00721938>.
- [36] C.B. Ponton, R.D. Rawlings, Vickers indentation fracture toughness test Part 1 Review of literature and formulation of standardised indentation toughness equations, *Mater. Sci. Technol.* 5 (1989) 865–872, <https://doi.org/10.1179/mst.1989.5.9.865>.
- [37] M. Krüger, P. Jain, K.S. Kumar, M. Heilmaier, Correlation between microstructure and properties of fine grained Mo-Mo<sub>3</sub>Si-Mo<sub>5</sub>SiB<sub>2</sub> alloys, *Intermetallics* 48 (2014) 10–18, <https://doi.org/10.1016/j.intermet.2013.10.025>.
- [38] M. Krüger, S. Franz, H. Saage, M. Heilmaier, J.H. Schneibel, P. Jéhanho, M. Böning, H. Kestler, Mechanically alloyed Mo-Si-B alloys with a continuous  $\alpha$ -Mo matrix and improved mechanical properties, *Intermetallics* 16 (2008) 933–941, <https://doi.org/10.1016/j.intermet.2008.04.015>.
- [39] C.A. Nunes, R. Sakidja, Z. Dong, J.H. Perepezko, Liquidus projection for the Mo-rich portion of the Mo-Si-B ternary system, *Intermetallics* 8 (2000) 327–337, [https://doi.org/10.1016/S0966-9795\(99\)00088-6](https://doi.org/10.1016/S0966-9795(99)00088-6).
- [40] O.C. Hellman, J.A. Vandenbroucke, J. Rüsing, D. Isheim, D.N. Seidman, Analysis of three-dimensional atom-probe data by the proximity histogram, *Microsc. Microanal.* 6 (2000) 437–444, [http://journals.cambridge.org/article\\_S1431927602000740](http://journals.cambridge.org/article_S1431927602000740). (Accessed 6 June 2017).
- [41] L. Mancini, N. Amirifar, D. Shinde, I. Blum, M. Gilbert, A. Vella, F. Vurpillot, W. Lefebvre, R. Lardé, E. Talbot, P. Pareige, X. Portier, A. Ziani, C. Davesne, C. Durand, J. Eymery, R. Butté, J.-F. Carlin, N. Grandjean, L. Rigutti, Composition of wide bandgap semiconductor materials and nanostructures measured by atom probe tomography and its dependence on the surface electric field, *J. Phys. Chem. C* 118 (2014) 24136–24151, <https://doi.org/10.1021/jp5071264>.
- [42] B. Gault, D.W. Saxey, M.W. Ashton, S.B. Sinnott, A.N. Chiramonti, M.P. Moody, D.K. Schreiber, Behavior of molecules and molecular ions near a field emitter, *N. J. Phys.* 18 (2016) 033031, <https://doi.org/10.1088/1367-2630/18/3/033031>.
- [43] W.C. Oliver, G.M. Pharr, An improved technique for determining hardness and elastic modulus using load and displacement sensing indentation experiments, *J. Mater. Res.* 7 (1992) 1564–1583, <https://doi.org/10.1557/JMR1992.1564>.
- [44] S. Majumdar, A. Kumar, D. Schliephake, H.-J. Christ, X. Jiang, M. Heilmaier, Microstructural and micro-mechanical properties of Mo-Si-B alloyed with Y and La, *Mater. Sci. Eng., A* 573 (2013) 257–263, <https://doi.org/10.1016/j.msea.2013.02.053>.
- [45] M. Göken, R. Sakidja, W.D. Nix, J.H. Perepezko, Microstructural mechanical properties and yield point effects in Mo alloys, *Mater. Sci. Eng., A* 319 (2001) 902–908, [https://doi.org/10.1016/S0921-5093\(01\)01086-3](https://doi.org/10.1016/S0921-5093(01)01086-3).
- [46] Y.W. Bao, W. Wang, Y.C. Zhou, Investigation of the relationship between elastic modulus and hardness based on depth-sensing indentation measurements, *Acta Mater.* 52 (2004) 5397–5404, <https://doi.org/10.1016/j.actamat.2004.08.002>.
- [47] Y. Yang, H. Bei, J. Tiley, E.P. George, Re effects on phase stability and mechanical properties of MoSS+Mo<sub>3</sub>Si+Mo<sub>5</sub>SiB<sub>2</sub> alloys, *J. Alloy. Comp.* 556 (2013) 32–38, <https://doi.org/10.1016/j.jallcom.2012.12.047>.
- [48] K. Ihara, K. Ito, K. Tanaka, M. Yamaguchi, Mechanical properties of Mo<sub>5</sub>SiB<sub>2</sub> single crystals, *Mater. Sci. Eng., A* 329 (2002) 222–227, [https://doi.org/10.1016/S0921-5093\(01\)01575-1](https://doi.org/10.1016/S0921-5093(01)01575-1).
- [49] R.O. Ritchie, Mechanisms of fatigue crack propagation in metals, ceramics and composites: role of crack tip shielding, *Mater. Sci. Eng., A* 103 (1988) 15–28, [https://doi.org/10.1016/0025-5416\(88\)90547-2](https://doi.org/10.1016/0025-5416(88)90547-2).
- [50] R.O. Ritchie, Mechanisms of fatigue-crack propagation in ductile and brittle solids, *Int. J. Fract.* 100 (1999) 55–83, <https://doi.org/10.1023/A:1018655917051>.